INTERNATIONAL JOURNAL FOR NUMERICAL METHODS IN FLUIDS, VOL. 24, 81–100 (1997)

# BEM SOLUTION OF THE 3D INTERNAL NEUMANN PROBLEM AND A REGULARIZED FORMULATION FOR THE POTENTIAL VELOCITY GRADIENTS

ADRIN GHARAKHANI AND AHMED F. GHONIEM

*Department of Mechanical Engineering, Massachusetts Institute of Technology, Cambridge, MA 02139, U.S.A.*

## SUMMARY

The direct boundary element method is an excellent candidate for imposing the normal flux boundary condition in vortex simulation of the three-dimensional Navier–Stokes equations. For internal flows, the Neumann problem governing the velocity potential that imposes the correct normal flux is ill-posed and, in the discrete form, yields a singular matrix. Current approaches for removing the singularity yield unacceptable results for the velocity and its gradients. A new approach is suggested based on the introduction of a pseudo-Lagrange multiplier, which redistributes localized discretization errors—endemic to collocation techniques—over the entire domain surface, and is shown to yield excellent results. Additionally, a regularized integral formulation for the velocity gradients is developed which reduces the order of the integrand singularity from four to two. This new formulation is necessary for the accurate evaluation of vorticity stretch, especially as the evaluation points approach the boundaries. Moreover, to guarantee second-order differentiability of the boundary potential distribution, a piecewise quadratic variation in the potential is assumed over triangular boundary elements. Two independent node-numbering systems are assigned to the potential and normal flux distributions on the boundary to account for the single- and multi-valuedness of these variables, respectively. As a result, higher accuracy as well as significantly reduced memory and computational cost is achieved for the solution of the Neumann problem.

KEY WORDS: boundary element; velocity; gradients

## INTRODUCTION

Vortex methods are a class of approximation techniques for the grid-free simulation of the unsteady, incompressible, high-Reynolds-number Navier–Stokes equations in external and internal flows. In this approach the governing equations are expressed in the vorticity transport form and the solution is obtained in terms of the trajectories of a large number of discrete vortex elements.

To simulate wall-bounded flow in three dimensions, the velocity field induced by the vortex elements is first obtained in an unbounded domain and then modified to satisfy the normal and tangential velocity boundary conditions on the walls.[1] For this purpose the normal flux boundary condition is applied by superimposing a wall-bounded potential flow over the vorticity-induced velocity field, and the slip velocity induced at the walls is anulled by generating vortex tiles (flat vortex elements) at the walls, with strength per unit length equal to the slip velocity. Convection of vorticity is evaluated, with minimal numerical diffusion, by tracking the trajectories of the vortex

CCC 0271–2091/97/010081–20

*Received 2 March 1995*
*Revised 15 April 1996*

elements in a Lagrangian form, using the total velocity at the element centre. Simulation of viscous diffusion in the random vortex method is obtained stochastically by the random walk method, exploiting the similarity between the Gaussian probability distribution function and the Green function for the diffusion equation. In addition, the vorticity vector associated with each element is modified by stretch, which is caused by the interaction between the vorticity and velocity gradients at the element location. A detailed formulation of the numerical algorithm and its application to various problems is beyond the scope of this paper;[1] instead we focus on attaining an accurate solution for the internal potential flow problem—a task that is critical to the success of the vortex–boundary element method.

The starting point for obtaining the potential velocity field in the vortex method is the Helmholtz decomposition of the velocity vector into vortical and potential components.[2] Given a distribution of vortex elements, the vortical component is evaluated in free space using the well-known Biot–Savart law.[2] Since the vortical velocity is divergence-free, pointwise satisfaction of continuity (or the incompressibility constraint) yields a Laplace equation that defines the flow due to the potential component. The boundary condition for the Laplace equation is expressed in terms of the normal flux at the boundary, which is evaluated as the difference between the normal flux boundary condition prescribed for the Navier–Stokes problem and the normal flux induced by the vortical velocity at the boundary. Subsequent to the solution of the Neumann problem, the potential velocity and its gradients are evaluated at the vortex element locations and used to convect and stretch the vortex elements in the interior, respectively. We obtain the potential flow for the interior using the direct boundary element method in order to preserve the grid-free nature of the random vortex method.

The solution of the three-dimensional Laplace equation by the classical boundary element method is by now an academic exercise, examples of which can be found in any reference book on the method.[3] Briefly, the boundary element method converts the differential description for the variation of the potential within the domain interior into a surface integral formulation, which links the boundary potential and its normal flux to the potential at an arbitrary point in the domain. Coalescing the interior point onto the boundary, applying the normal flux boundary condition for the Neumann problem and solving the resulting integral equation yields the unknown boundary potential distribution. Note that the Neumann problem is analytically ill-posed and the potential solution is valid only up to a constant; nevertheless, the potential velocity and its gradients are uniquely defined.

The accurate evaluation of the velocity in the domain is currently an active area of research. In the conventional form the velocity of an interior point is evaluated by directly differentiating the standard boundary integral equation[3] and is therefore a function of the distributions of the potential and its normal flux on the boundary. The integrals in this formulation contain third-order singularities, which lead to a poor approximation of the velocity near the boundary and infinite values at the boundary. A regularized form of the velocity integrals is available which reduces the order of the singularity by one and hence improves the quality of the approximations in the interior of the domain significantly—excluding the boundary where the integrals are still infinitely large.[4] The regularized form of the velocity was later extended to a desingularized integral equation which is accurate everywhere in the domain, including the boundary.[5,6] It should be mentioned here that both regularized and desingularized versions of the velocity integral are dependent on the distributions of the normal flux and the *tangential derivatives* of the potential at the boundary. Since the standard Neumann solution yields the potential distribution, the corresponding tangential derivatives are obtained by differentiating the computed potential distribution. Therefore, the accuracy of the tangential velocities is at best equal to and generally less than that of the potential solution.

More recently, a similar desingularized formulation was developed which couples the velocity in the domain interior to the normal flux and the two tangential derivatives of the potential on the boundary.[7] The advantage of the new method is that it is capable of bypassing the prerequisite of

evaluating the boundary potential, by solving the Neumann problem directly in terms of the tangential derivatives of the boundary potential. Therefore, questions regarding the ill-posedness of the Neumann problem as well as concerns related to the differentiation of the numerical potential distribution are eliminated. However, this approach is computationally too intensive as it is necessary to solve two coupled integral equations for the two components of the tangential velocities at the walls.

In this paper, we examine two problems related to the application of the boundary element method to obtain the potential flow inside a three-dimensional domain, which, to the best of our knowledge, have not been attempted in the past. First, we present the solution of the analytically ill-posed Neumann problem. We use two standard methods for removing the matrix singularity associated with the discretized Neumann problem and show that the potential distributions on the boundary are accompanied by spikes—in turn contaminating the potential flow inside the domain. We propose an alternative method which is based on the introduction of a pseudo-Lagrange multiplier that redistributes the localized discretization errors over the entire domain boundary. We show that this approach yields excellent results on the boundary as well as in the interior. Secondly, we develop a regularized integral formulation for evaluating the velocity gradients at arbitrary points in the domain. In this approach the integrand singularity is reduced by two orders as compared with the classical formulation, significantly improving the velocity gradient estimates near the boundaries. Since the reduction in the singularity order by two requires the potential on the boundary to be twice-differentiable, we asign a piecewise quadratic variation to the potential and its normal flux over planar triangular elements. We extend the exact singular integration algorithm of Medina and Liggett[8] for the linear variation of the potential over flat triangular elements to the case of a quadratic variation and list the formulae in the Appendix. Finally, we propose one node numbering system for the variation of the single-valued potential on the boundary; and another node numbering system, independent of the former, which takes the multi-valuedness of the normal flux at the boundary edges and corners into account. This approach maintains an accurate solution of the boundary potential and requires significantly lower computational cost and memory. We verify the accuracy of the developed methodologies using a test problem of flow inside a cube having parabolic inlet and flat exit velocity profiles and compare the results with the analytical solutions.

## FORMULATION

The Neumann problem describing the potential distribution $\Phi(\mathbf{x})$ inside a domain of interest $\Omega$, with boundary $\partial\Omega$, is given by

$$\nabla^2\Phi(\mathbf{x}) = 0, \quad \mathbf{x} \in \Omega, \tag{1a}$$

$$q(\boldsymbol{\chi}) = \nabla\Phi(\boldsymbol{\chi}) \cdot \mathbf{n}, \quad \boldsymbol{\chi} \in \partial\Omega, \tag{1b}$$

$$\int_{\partial\Omega} q(\boldsymbol{\chi})\, \mathrm{d}S(\boldsymbol{\chi}) = 0, \tag{1c}$$

where $S(\boldsymbol{\chi})$ is the surface area of the boundary and $\mathbf{n} = (n_x, n_y, n_z)$ is the unit outward normal to it. Constraint (1c) enforces a zero net flux into the domain and is a necessary condition for the Neumann solution to exist. This implies that boundary condition (1b) is overspecified, because the flux at any arbitrary point $\boldsymbol{\chi}_0$ on the boundary may be written in terms of the flux at other points.

Therefore, the Neumann problem is solvable only up to a constant in the potential at $\boldsymbol{\chi}_0$, which can arbitrarily be set to zero in the current problem since only the derivatives of the field potential are of interest here:

$$\Phi(\boldsymbol{\chi}_0) = 0. \tag{1d}$$

## SOLUTION

*Matrix assembly*

The Laplace equation can be reformulated in the following boundary integral form[3]:

$$\Phi(\mathbf{x})\alpha(\mathbf{x}) = -\int_{\partial\Omega} \Phi(\boldsymbol{\chi})F(\boldsymbol{\chi}, \mathbf{x})\, \mathrm{d}S(\boldsymbol{\chi}) + \int_{\partial\Omega} G(\boldsymbol{\chi}, \mathbf{x})q(\boldsymbol{\chi})\, \mathrm{d}S(\boldsymbol{\chi}), \tag{2}$$

where $G(\boldsymbol{\chi}, \mathbf{x}) = G(r) = 1/4\pi r$ is the three-dimensional Green function, $F(\boldsymbol{\chi}, \mathbf{x}) = \nabla G(\boldsymbol{\chi}, \mathbf{x}) \cdot \mathbf{n} = G_{,i} n_i$ is its normal flux and

$$\alpha(\mathbf{x}) = \begin{cases} 1, & \mathbf{x} \in (\Omega \backslash \partial\Omega), \\ -\displaystyle\int_{\partial\Omega} F(\boldsymbol{\chi}, \mathbf{x})\, \mathrm{d}S(\boldsymbol{\chi}), & \mathbf{x} \in \partial\Omega, \\ 0, & \mathbf{x} \notin \Omega. \end{cases}$$

In addition,

$$G_{,i} = \frac{-r_{,i}}{4\pi r^2}, \qquad r_{,i} = \frac{r_i}{r}, \qquad r = \sqrt{(r_i r_i)}, \qquad r_i = \chi_i - x_i \qquad i = 1, 2, 3$$

where Einstein's rule for indices is used and the differentiation is performed with respect to $\chi_i$. For simplicity, in what follows, references to independent variables in the integral equations will be ignored, unless it is explicitly necessary.

Equation (2) can be discretized by decompong $\partial\Omega$ into a union of $K$ surfaces such that $\partial\Omega = \sum_{k=1}^{K} \partial\Omega_k$, and by approximating the potential and normal flux distributions on the boundary by a set of piecewise smooth polynomials. The accuracy of the approximation depends upon the proper discretization of the curved boundary surfaces, the correct representation of $\Phi$ and $q$ distribution functions, and the accurate evaluation of the singular integrals. In this paper we present our results with minimum numerical bias by considering geometries with planar surfaces and by evaluating the singular integrations analytically. Furthermore, we assign piecewise quadratic interpolation functions to the variation of the potentials and fluxes across each element. Consequently, the solution is primarily controlled by the grid resolution and distribution.

The exact integration algorithm proposed by Medina and Liggett[8] for linear interpolation functions over flat triangular elements is herein extended to the case of quadratic functions over the elements. In addition to yielding more accurate results than their linear counterparts (for the same number of nodes), quadratic interpolation functions are a minimum necessity in the present analysis. This is because, as will be shown shortly, the regularized formulation for the velocity gradients requires the boundary potential distribution to be at least twice-differentiable. Thus, the latter must be approximated by at least a quadratic interpolation function. Note that it is possible to obtain superlinear convergence for the velocity gradients using linear interpolation functions for the potential distribution. However, in this case the treatment of the edges and corners is tricky and its discussion is avoided here.[9] The boundary surface is described by a collection of $K$ plane triangular elements, and a local orthonormal co-ordinate system $\xi$–$\zeta$–$\eta$ is assigned to each element as depicted

in Figure 1. The corresponding unit vectors are represented by $\boldsymbol{\tau}$–$\boldsymbol{\rho}$–$\mathbf{n}$, where $\boldsymbol{\tau} = (\tau_x, \tau_y, \tau_z)$ and $\boldsymbol{\rho} = (\rho_x, \rho_y, \rho_z)$. The origin of each co-ordinate system is positioned at $\mathbf{x}$, while its orientation is set such that $\boldsymbol{\tau}$–$\boldsymbol{\rho}$ is parallel to the element plane, and $\boldsymbol{\tau}$ is along the longest side of the triangle and in the direction which is consistent with the outward normal $\mathbf{n}$:

$$\Phi(\mathbf{x})\alpha(\mathbf{x}) = \sum_{k=1}^{K} \left( \eta_k \int_{\partial\Omega_k} \frac{\Phi^k(\xi, \zeta)}{4\pi r_k^3} \, \mathrm{d}S_k + \int_{\partial\Omega_k} \frac{q^k(\xi, \zeta)}{4\pi r_k} \, \mathrm{d}S_k \right), \tag{3}$$

where $r_k$ is the distance between the field point $\mathbf{x}$ and points on boundary element $k$, and $\eta_k$ is its normal projection $\mathbf{n} \cdot (\boldsymbol{\chi}_k - \mathbf{x})$. The quadratic variation of $\Phi$ (or $q$) over element $k$ is formulated in the form $f^k(\xi, \zeta) = c^k_{1,f} + c^k_{2,f}\xi + c^k_{3,f}\zeta + c^k_{4,f}\xi\zeta + c^k_{5,f}\xi^2 + c^k_{6,f}\zeta^2$. (Here, $f^k(\xi, \zeta)$ is a dummy variable representing $\Phi$ or $q$.) Taking into account the orientation of the local co-ordinate system, the coefficients $c$ for element $k$ may be obtained by the following, somewhat less complicated, formula:

$$\begin{pmatrix} c_{1,f} \\ c_{2,f} \\ c_{3,f} \\ c_{4,f} \\ c_{5,f} \\ c_{6,f} \end{pmatrix} = \begin{pmatrix} 1 & \xi_1 & \zeta_1 & \xi_1\zeta_1 & \xi_1^2 & \zeta_1^2 \\ 1 & \xi_2 & \zeta_1 & \xi_2\zeta_1 & \xi_2^2 & \zeta_1^2 \\ 1 & \xi_3 & \zeta_3 & \xi_3\zeta_3 & \xi_3^2 & \zeta_3^2 \\ 1 & \xi_4 & \zeta_1 & \xi_4\zeta_1 & \xi_4^2 & \zeta_1^2 \\ 1 & \xi_5 & \zeta_5 & \xi_5\zeta_5 & \xi_5^2 & \zeta_5^2 \\ 1 & \xi_6 & \zeta_5 & \xi_6\zeta_5 & \xi_6^2 & \zeta_5^2 \end{pmatrix}^{-1} \begin{pmatrix} f(\xi_1, \zeta_1) \\ f(\xi_2, \zeta_1) \\ f(\xi_3, \zeta_3) \\ f(\xi_4, \zeta_1) \\ f(\xi_5, \zeta_5) \\ f(\xi_6, \zeta_5) \end{pmatrix},$$

where

$$\xi_4 = \frac{\xi_1 + \xi_2}{2}, \qquad \xi_5 = \frac{\xi_2 + \xi_3}{2}, \qquad \xi_6 = \frac{\xi_1 + \xi_3}{2}, \qquad \zeta_5 = \frac{\zeta_1 + \zeta_3}{2}$$

and the indices for $\xi$ and $\zeta$ refer to the local node numbering system of Figure 1. The nodal values of $\Phi$ and $q$ at the local level are in turn linked to a global node numbering system. Substituting the

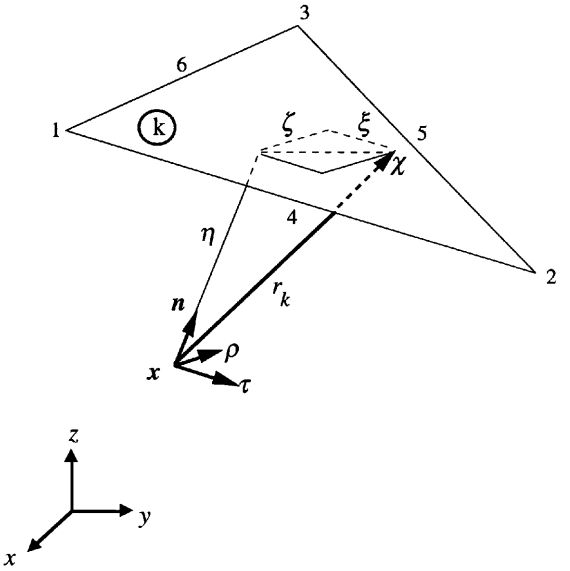


Figure 1. Schematic diagram depicting the co-ordinate system and node numbering of a typical boundary element

interpolation functions into equation (3) leads to the following boundary element approximation of equation (2):

$$\alpha(\mathbf{x})\Phi(\mathbf{x}) - \sum_{k=1}^{K}(c_{1,\Phi}^{k}I^{3,k} + c_{2,\Phi}^{k}I_{\xi}^{3,k} + c_{3,\Phi}^{k}I_{\zeta}^{3,k} + c_{4,\Phi}^{k}I_{\xi\zeta}^{3,k} + c_{5,\Phi}^{k}I_{\xi^2}^{3,k} + c_{6,\Phi}^{k}I_{\zeta^2}^{3,k})\eta_k$$
$$= \sum_{k=1}^{K}(c_{1,q}^{k}I^{1,k} + c_{2,q}^{k}I_{\xi}^{1,k} + c_{3,q}^{k}I_{\zeta}^{1,k} + c_{4,q}^{k}I_{\xi\zeta}^{1,k} + c_{5,q}^{k}I_{\xi^2}^{1,k} + c_{6,q}^{k}I_{\zeta^2}^{1,k}), \tag{4}$$

where $4\pi I_{\xi^i\zeta^j}^{m,k} \equiv \int_{\partial\Omega_k} \dfrac{\xi^i\zeta^j}{r_k^m}\,\mathrm{d}S_k$ are listed in the Appendix.

Note that while the potential distribution is single-valued everywhere on the boundary, its normal flux is multi-valued on the edges and corners. This poses difficulties in assigning the link between the local and global node numbers. To this end, the multiple-node concept[3]—assigning as many nodes to a point on an edge (or a corner) as there are surfaces sharing the edge (or the corner)—may be implemented to describe the normal flux uniquely everywhere on the boundary. However, extending this concept to describe the boundary potential may incorrectly yield different potential values for the same location on an edge or a corner because of round-off and discretization errors. Moreover, an increase in the number of nodes, due to the assignment of multiple nodes to both $\Phi$ and $q$, will unnecessarily increase the memory requirement as well as the computational cost by a considerable amount. We propose the implementation of two separate global node numbering systems for $\Phi$ and $q$. The first is used to describe the potential distribution over $N$ global nodes in the regular sense, while the second utilizes the multiple-node prescription to assign the normal flux over $M$ global nodes. Additionally, the $N$ potential nodes are linked to the $M$ normal flux nodes by a simple indexing system.

Coalescing $\mathbf{x}$ with each of the $N$ collocation nodes that define the potential distribution in equation (4), carrying out the singular integration over the boundary elements and collecting like terms sets up a linear system of equations for the $N$ unknown potentials at the nodes:

$$\sum_{j=1}^{N} a_{ij}\Phi_j = \sum_{j=1}^{M} b_{ij}q_j, \quad i = 1, \ldots, N,$$
$$a_{ii} = -\sum_{\substack{j=1 \\ j\neq i}}^{N} a_{ij}, \tag{5}$$

where $a_{ii}$ is the solid angle $\alpha(\mathbf{x})$ on each of the $N$ collocation nodes.

*Matrix conditioning*

In equation (5), matrix $a_{ij}$ is singular and cannot be inverted without considering constraint (1d). Three approaches are presented herein for removing the singularity.

Method 1, the elimination or penalty method, is widely used in the finite element method. In this approach, constraint (1d) is applied by setting the potential at an arbitrary collocation point $m$ equal to zero and eliminating its corresponding equation. Note that by problem definition, constraint (1c) is also satisfied. Thus

$$\sum_{j=1}^{N} a_{ij}\Phi_j = \sum_{j=1}^{M} b_{ij}q_j, \quad i = 1, \ldots, m-1, m+1, \ldots, N. \tag{6}$$

In Method 2, the Laplace equation is evaluated as a degenerate mixed Dirichlet–Neumann problem, where the normal flux at an arbitrary collocation point $p$ is temporarily assumed to be unknown and its contribution to the system is moved to the left of equation (5). The potential $\Phi_m$ at

that same point is assumed to be known and equal to zero, thus satisfying constraint (1d). Note that $p$ and $m$ reflect the two node numbering systems for the same physical location and that $b_{ip}q_p$ substitutes $a_{im}\Phi_m$ in equation (7). The advantage of this method is that by solving for the 'unknown' $q$, the singularity of matrix $a_{ij}$ is automatically removed. However, constraint (1c) is not strictly enforced and the value of the normal flux at $p$, obtained from the solution of equation (7), may not be equal to its originally specified value:

$$\sum_{\substack{j=1\\ j\neq m}}^{N} a_{ij}\Phi_j - b_{ip}q_p = \sum_{\substack{j=1\\ j\neq p}}^{M} b_{ij}q_j, \quad i = 1, \ldots, N. \tag{7}$$

Barring round-off errors, the first and second methods are expected to yield identically accurate results in the limit of infinitely fine discretizations of $\Phi$ and $q$. However, computationally, both methods are severely limited, not only by grid density but also by how the grids are distributed. Also, as will be demonstrated in the Results section, an impractically large number of grid points may be necessary to obtain a reasonably accurate solution, especially near the edges and corners.

Method 3, which we propose to remedy this problem, is a variation on the pseudo-Lagrange multiplier idea which was utilized earlier in coupled boundary element and finite element problems.[10] It is motivated by the collocation properties of the boundary element method. That is, solutions obtained by the boundary element method are grid-dependent and local residual errors caused by machine precision and insufficient discretization may produce spikes in the solutions. Therefore, a Lagrange multiplier is added to the system of equations to equilibrate the imbalance between its left and right sides, by scaling and redistributing the residual errors on an area-weighted basis. The value of the Lagrange multiplier is determined as an unknown of the system.

In the original implementation of this approach, where the solution of mixed Dirichlet-Neumann problems was sought, constraint (1c) was strictly enforced by including it in the linear system (5) as a supplementary equation.[10] The addition of the constraint perturbs the balance of equations (5). In this case the role of the Lagrange multiplier is to introduce a controlled error into each of equations (5) as a tuning mechanism which redistributes the normal flux on the boundary.

In the present implementation of this method the idea of distributing controlled errors is similar to that of the original version; however, the similarity ends here. In Method 3, a Lagrange multiplier is added to each of the $N$ equations (5) to control the equilibrium between the left and right sides on an area-weighted basis, leading to a system of $N$ equations and $N+1$ unknowns. Thus, an additional equation is required to solve for the multiplier as a new extra unknown of the problem. For the Neumann problem, where the normal flux is known everywhere, constraint (1c) is satisfied by construction and is no longer available as an extra equation. On the other hand, constraint (1d) may be exploited to *reduce* the number of unknowns by one to $N$—the number of available equations. That is, the potential at an arbitrary collocation point $m$ is treated as a known quantity and set equal to zero. Note that, unlike in the elimination method, equation $m$ corresponding to $\Phi_m$ is not removed from the system. Thus, the new system of equations is

$$\sum_{\substack{j=1\\ j\neq m}}^{N} a_{ij}\Phi_j + d_i\lambda = \sum_{j=1}^{M} b_{ij}q_j, \quad i = 1, \ldots, N, \tag{8}$$

where $\lambda$ is the Lagrange multiplier (and is usually small.) To obtain $d_i$, $\lambda$ is first assigned a piecewise quadratic variation over plane triangular elements and its distribution integrated over the surface:

$$\sum_{k=1}^{K} \int_{\partial\Omega_k} (c^k_{1,\lambda} + c^k_{2,\lambda}\xi + c^k_{3,\lambda}\zeta + c^k_{4,\lambda}\xi\zeta + c^k_{5,\lambda}\xi^2 + c^k_{6,\lambda}\zeta^2)\, \mathrm{d}S_k.$$

Carrying out the integration and simplifying yields

$$\sum_{k=1}^{K}\sum_{j=4}^{6}\frac{S_k}{3}\lambda^{k,j}=\sum_{k=1}^{K}\sum_{j=4}^{6}d^{k,j}\lambda^{k,j},$$

where $(.)^{k,j}$ is the index notation which connects the local $j$th node number of element $k$ to the global node number $i$ at that point. Note that each of nodes 4, 5 and 6—at the centres of the three sides of triangle $k$—contributes a third of the boundary element area to the value of $d^{k,j}$, while the vertices do not contribute at all. Now, $d_i$ can be evaluated by summing the area contributions from all boundary elements that share node $i$ and by setting $\lambda_i=\lambda$.

*Velocities and their gradients at internal points*

Having solved for $\Phi(\boldsymbol{\chi})$ on the boundary, the velocity at arbitrary internal points may be obtained by differentiating equation (2) directly:

$$u_j(\mathbf{x})=-\frac{\partial\Phi(\mathbf{x})}{\partial x_j}=-\int_{\partial\Omega}\Phi F_{,j}\,\mathrm{d}S+\int_{\partial\Omega}G_{,j}q\,\mathrm{d}S,\quad j=1,2,3, \tag{9}$$

where $F_{,j}=G_{,ij}n_i$, $G_{,ij}=(1/4\pi r^3)(3r_{,i}r_{,j}-\delta_{ij})$ and $\delta_{ij}$ is the Kronecker delta.

Equation (9) contains an $r^{-3}$ integrand singularity which yields in accurate velocity values as the evaluation point approaches the boundary. Balas *et al.*[4] introduced a novel regularization technique in which the singularity is reduced by one order in exchange for evaluating the tangential derivatives of the potential on the boundaries. The regularized formula is reproduced here in its final form:

$$u_j(\mathbf{x})=\int_{\partial\Omega}G_{,i}[\varepsilon_{jim}(\tau_m\Phi_{,\zeta}-\rho_m\Phi_{,\xi})+\delta_{ij}q]\,\mathrm{d}S,\quad j=1,2,3, \tag{10}$$

where $\varepsilon_{ijm}$ is the antisymmetric permutation symbol.

The integral formulations for the velocities are now extended to obtain the corresponding velocity gradients at arbitrary internal points. The singular form of the velocity gradients is obtained by directly differentiating equation (9), which yields

$$\frac{\partial u_j(\mathbf{x})}{\partial x_l}=\int_{\partial\Omega}\Phi F_{,jl}\,\mathrm{d}S-\int_{\partial\Omega}G_{,jl}q\,\mathrm{d}S,\quad (j,l)=1,2,3, \tag{11}$$

where $F_{,jl}=G_{,ijl}n_i$ and $G_{,ijl}=(3/4\pi r^4)(-5r_{,i}r_{,j}r_{,l}+\delta_{ij}r_{,l}+\delta_{il}r_{,j}+\delta_{jl}r_{,i})$.

The singularity in equation (11) is of the order of $r^{-4}$ and the accuracy of the velocity gradient integrals deteriorates very rapidly as the arbitrary points approach the boundary, and the integrals cease to exist at the boundary. The regularized form of the velocity gradients may be obtained by differentiating equation (10):

$$\frac{\partial u_j(\mathbf{x})}{\partial x_l}=-\int_{\partial\Omega}G_{,il}[\varepsilon_{jim}(\tau_m\Phi_{,\zeta}-\rho_m\Phi_{,\xi})+\delta_{ij}q]\,\mathrm{d}S,\quad (j,l)=1,2,3. \tag{12}$$

Although the integrand singularity in equation (12) has been reduced by one order, the solution near the boundary is still quite poor and further reduction of the singularity to order $r^{-2}$ is desirable. Application of the chain rule for differentials and Gauss' theorem to equation (12) and further simplification leads to the lower-order integral

$$\frac{\partial u_j(\mathbf{x})}{\partial x_l}=\int_{\partial\Omega}G_{,i}[\varepsilon_{jim}(\tau_m\Phi_{,\zeta}-\rho_m\Phi_{,\xi})+\delta_{ij}q]_{,l}\,\mathrm{d}S,\quad (j,l)=1,2,3. \tag{13}$$

Rewriting the Laplace equation in local co-ordinates, $\Phi_{,\eta\eta} = -(\Phi_{,\xi\xi} + \Phi_{,\zeta\zeta})$, and recalling that $q = \Phi_{,\eta}$, the derivatives in the $l$th direction in equation (13) may be formulated as

$$\begin{aligned} \Phi_{,\xi l} &= \Phi_{,\xi\xi}\tau_l + \Phi_{,\xi\zeta}\rho_l + q_{,\xi}n_l, \qquad \Phi_{,\zeta l} = \Phi_{,\xi\zeta}\tau_l + \Phi_{,\zeta\zeta}\rho_l + q_{,\zeta}n_l, \\ q_{,l} &= q_{,\xi}\tau_l + q_{,\zeta}\rho_l - (\Phi_{,\xi\xi} + \Phi_{,\zeta\zeta})n_l, \qquad l = 1, 2, 3. \end{aligned} \tag{14}$$

Substituting equations (14) into equation (13) yields the final form of the regularized velocity gradient integrals:

$$\begin{aligned} \frac{\partial u_j(\mathbf{x})}{\partial x_l} = \int_{\partial\Omega} G_{,i}\{&\varepsilon_{jim}[\tau_m\rho_l\Phi_{,\zeta\zeta} - \tau_l\rho_m\Phi_{,\xi\xi} + (\tau_l\tau_m - \rho_l\rho_m)\Phi_{,\xi\zeta} + (\tau_m q_{,\zeta} - \rho_m q_{,\xi})n_l] \\ &+\delta_{ij}[\tau_l q_{,\xi} + \rho_l q_{,\zeta} - (\Phi_{,\xi\xi} + \Phi_{,\zeta\zeta})n_l]\}\, \mathrm{d}S, \quad (j, l) = 1, 2, 3. \end{aligned} \tag{15}$$

We now proceed with the discretization of equations (10) and (15) over the $K$ plane triangular elements. Note that $G_{,i}$ can be written in terms of our local co-ordinate system as

$$G_{,i} = \frac{-(\xi\tau_i + \zeta\rho_i + \eta n_i)}{4\pi r^3}, \quad i = 1, 2, 3. \tag{16}$$

The discretized velocities are arrived at by combining equations (10) and (16) and by further simplifying the result using the properties of the permutation symbol:

$$\begin{aligned} u_j(\mathbf{x}) = \sum_{k=1}^{K} \Bigg\{ \int_{\partial\Omega_k} &[(\xi_k n_j - \eta_k\tau_j)\Phi^k_{,\xi}(\xi, \zeta) + (\zeta_k n_j - \eta_k\rho_j)\Phi^k_{,\zeta}(\xi, \zeta) \\ &- (\xi_k\tau_j + \zeta_k\rho_j + \eta_k n_j)q^k(\xi, \zeta)]\frac{\mathrm{d}S_k}{4\pi r_k^3} \Bigg\}, \quad j = 1, 2, 3. \end{aligned} \tag{17}$$

Similarly, equation (15) can now be discretized in the form

$$\begin{aligned} \frac{\partial u_j(\mathbf{x})}{\partial x_l} = \sum_{k=1}^{K} \Bigg( \int_{\partial\Omega_k} &\{[\xi_k(n_j\tau_l + \tau_j n_l) + \zeta_k\rho_j n_l + \eta_k(n_j n_l - \tau_j\tau_l)]\Phi^k_{,\xi\xi}(\xi, \zeta) \\ &+ [\zeta_k(n_j\rho_l + \rho_j n_l) + \xi_k\tau_j n_l + \eta_k(n_j n_l - \rho_j\rho_l)]\Phi^k_{,\zeta\zeta}(\xi, \zeta) \\ &+ [\xi_k n_j\rho_l + \zeta_k n_j\tau_l - \eta_k(\tau_j\rho_l + \rho_j\tau_l)]\Phi^k_{,\xi\zeta}(\xi, \zeta) \\ &+ [\xi_k(n_j n_l - \tau_j\tau_l) - \zeta_k\rho_j\tau_l - \eta_k(n_j\tau_l + \tau_j n_l)]q^k_{,\xi}(\xi, \zeta) \\ &+ [\zeta_k(n_j n_l - \rho_j\rho_l) - \xi_k\tau_j\rho_l - \eta_k(n_j\rho_l + \rho_j n_l)]q^k_{,\zeta}(\xi, \zeta)\} \frac{\mathrm{d}S_k}{4\pi r_k^3} \Bigg), \quad (j, l) = 1, 2, 3. \end{aligned} \tag{18}$$

In equations (17) and (18) the first and second derivatives of the boundary potential as well as the first derivatives of the normal flux may be obtained by several numerical approximation techniques, such as the least squares fit. In this paper, we evaluate these expressions by successive differentiation of the interpolation functions for $\Phi$ and $q$:

$$\begin{aligned} &\Phi^k_{,\xi}(\xi, \zeta) = c^k_{2,\Phi} + c^k_{4,\Phi}\zeta + 2c^k_{5,\Phi}\xi, \qquad \Phi^k_{,\zeta}(\xi, \zeta) = c^k_{3,\Phi} + c^k_{4,\Phi}\xi + 2c^k_{6,\Phi}\zeta, \\ &q^k_{,\xi}(\xi, \zeta) = c^k_{2,q} + c^k_{4,q}\zeta + 2c^k_{5,q}\xi, \qquad q^k_{,\zeta}(\xi, \zeta) = c^k_{3,q} + c^k_{4,q}\xi + 2c^k_{6,q}\zeta, \\ &\Phi^k_{,\xi\xi}(\xi, \zeta) = 2c^k_{5,\Phi}, \qquad \Phi^k_{,\zeta\zeta}(\xi, \zeta) = 2c^k_{6,\Phi}, \qquad \Phi^k_{,\xi\zeta}(\xi, \zeta) = c^k_{4,\Phi}. \end{aligned} \tag{19}$$

## RESULTS

The accuracy of the boundary element approximation presented above is now investigated by comparing the numerical results with the analytical solution of the potential flow inside a cube with unity dimensions. In particular, we demonstrate with this example the savings in memory and CPU time using the proposed node numbering approach, the effect of matrix conditioning on the accuracy of the boundary potential distribution and the flow field inside the domain, and the improvement in the accuracy of the velocity gradient profiles using the regularized integral formulation. We selected our test problem of flow in the cube (with the boundary conditions given below) because (i) an exact solution can be obtained by a standard separation of variables, and (ii) the flow is complicated enough (with discontinuous velocity gradient at the wall) to test the robustness of our proposed techniques. In what follows, the cube surfaces are taken to be normal to the $x$–$y$–$z$ global co-ordinate system, the origin is fixed at a corner of the exit surface and $z$ is parallel to and pointing opposite the flow direction. The components of the velocity are designated as $u$–$v$–$w$ in the $x$–$y$–$z$ direction, respectively. The normal flux boundary condition, satisfying constraint (1c), was set at

$$q(x, y, z = 1) = -6x(1 - x), \qquad q(x, y, z = 0) = 1, \qquad q(\text{elsewhere}) = 0.$$

The arbitrary reference point where constraint (1d) is satisfied was selected at (0·5, 0·5, 0·0)—the centre of the exit plane. Each surface of the cube was discretized into $4 \times 4$, $6 \times 6$ or $8 \times 8$ rectangular boundary elements and the elements were subsequently subdivided into two right triangles. Both uniform and non-uniform grid distributions were tested for each grid resolution, leading to a total of six cases. The non-uniform distribution was prescribed by a standard cosine function which tends to concentrate more nodes towards the edges.

Table I lists the total number of triangular boundary elements for each of the three resolutions as well as the number of collocation nodes for the potential and normal flux distributions. The percentage savings in memory and computational cost are also listed for the proposed node numbering scheme. Note that these values are not universal and depend on the configuration in question. For example, approximating the circular cross-sections of a suddenly expanding pipe by polygons leads to a configuration which has a large number of corners and edge points. As a result, the observed savings in memory and CPU time will be considerably higher than those presented in this paper.

The three matrix conditioning methods were applied to each of the six cases and the results are compared with the exact solution in Figures 2 and 3. Figures 2(a)–2(c) represent the solutions obtained by Methods 1–3, respectively, and depict the effect of grid resolution and distribution on the normalized potential distribution along station ($x$, 0·5, 0·0)—defined as $\Phi(x,0{\cdot}5,\ 0{\cdot}0)\Phi/\Phi(0{\cdot}5,\ 0{\cdot}5,\ 1{\cdot}0)$. Figure 2(d) shows the corresponding normal flux distribution obtained by Method 2. Two characteristics of Method 1 are immediately evident in Figure 2(a). First, potentials obtained by the uniform and non-uniform grid distributions are of opposite sign, with the latter having the same sign as the exact solution. Second, the potential distribution exhibits a spike at the reference point, with an amplitude that is four orders of magnitude larger than the average of the exact potential at the exit.

Table I

| Grid density | Number of elements | Number of Φ-nodes | Number of $q$-nodes | % memory savings | % CPU savings |
|---|---|---|---|---|---|
| $4 \times 4$ | 192 | 386 | 486 | 40 | 20 |
| $6 \times 6$ | 432 | 866 | 1014 | 26 | 20 |
| $8 \times 8$ | 768 | 1538 | 1734 | 20 | 16 |

Note that for the uniform grid distributions an increase in grid resolution leads to a significant reduction in the amplitude of the spikes. However, in the case of non-uniform grids, the influence of grid resolution is hardly noticeable. On the other hand, for a given grid resolution, non-uniform grids yield more accurate potentials than their uniform counterparts. Indeed, the solution obtained by the $4 \times 4$ non-uniform grid is more accurate than the one produced by the $8 \times 8$ uniform grid.

Method 2 also produces a spike at the reference point, but with an amplitude that is two orders of magnitude smaller than the one produced by Method 1. Additionally, the potentials obtained by uniform and non-uniform grids are of the same sign as the exact solution and are both sensitive to grid resolution. Figure 2(d) reveals that the apparent improvement in the potential distribution has been compromised by a spike in the normal flux distribution, which violates constraint (1c).

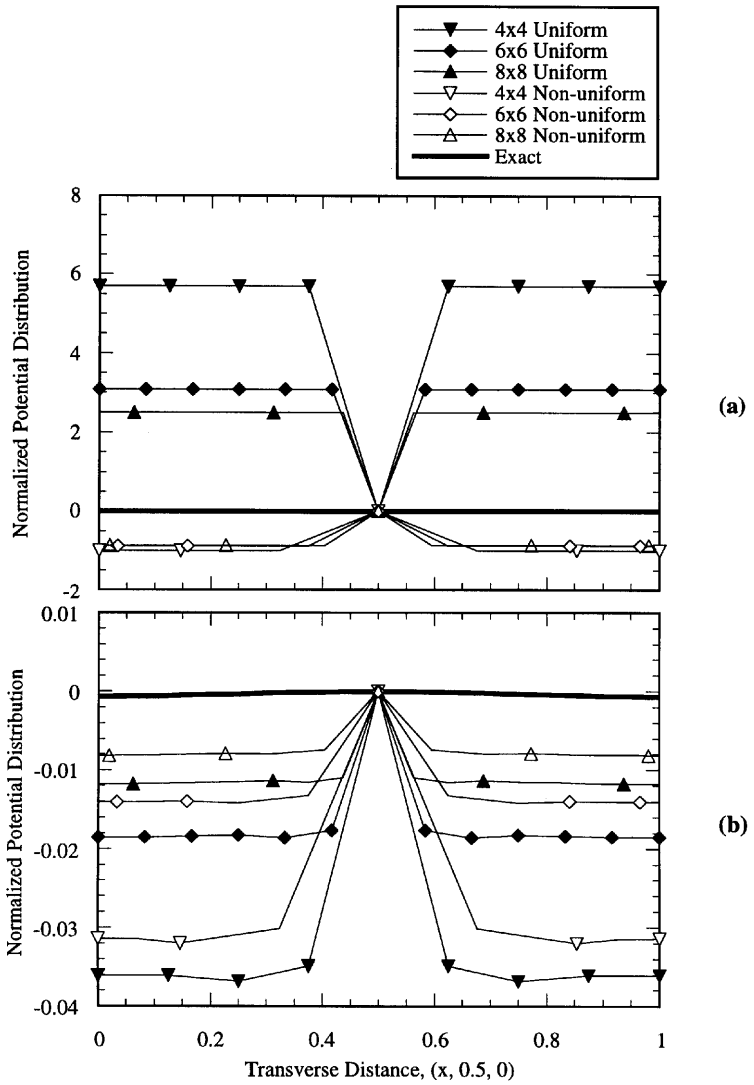


Figure 2. Parametric study of the effect of grid density and distribution on the solution of the Neumann problem, using three matrix conditioning techniques: (a) exit potential distribution using Method 1; (b) exit potential distribution using Method 2

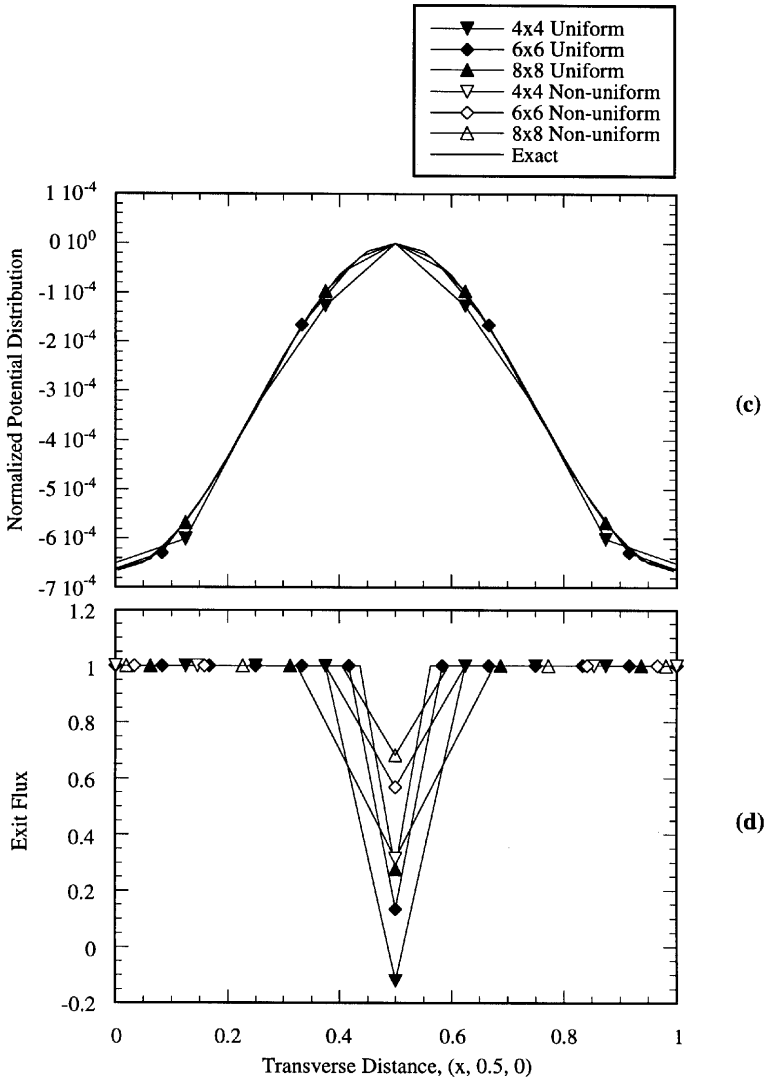


Figure 2. (continued) Parametric study of the effect of grid density and distribution on the solution of the Neumann problem, using three matrix conditioning techniques: (c) exit potential distribution using Method 3; (d) exit normal flux distribution using Method 2

The fundamental observation made from the parametric studies of Methods 1 and 2, despite their characteristic differences, is that a poor approximation of the potential and normal flux distributions on the boundary localizes the discretization error in the entire domain into a spike for the potential (and the flux) at the reference point. Increasing the grid resolution and concentrating more nodes closer to the edges should eventually remove the spike. However, it is clear from the plots that a prohibitively large number of grids may be necessary before an acceptable solution is obtained. Method 3 was proposed to remedy this problem and, as seen in Figure 2(c), it removes the spike even with the $4 \times 4$ uniform grid distribution, while at $8 \times 8$ grid resolution the approximation and the exact solution are indistinguishable.

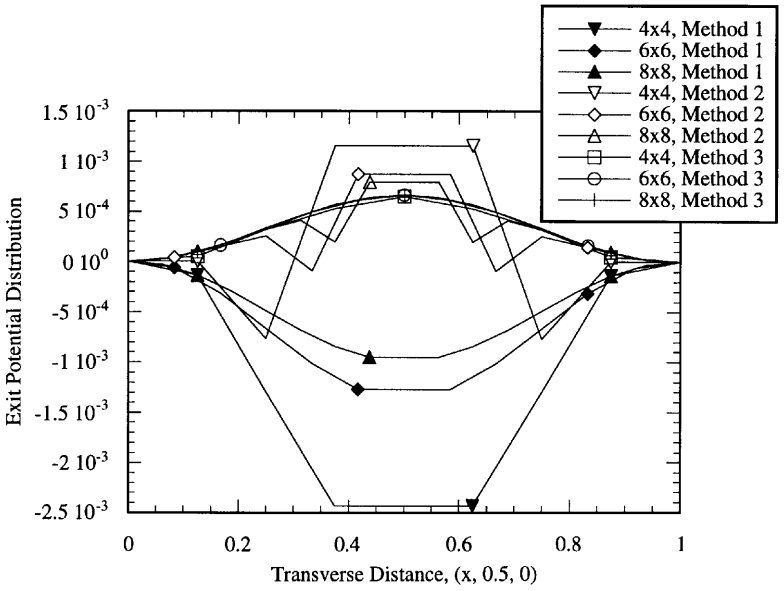


Figure 3. Close-up of the exit potential distribution obtained by Methods 1–3

Figure 3 depicts a close-up of the obtained solution using the three methods on uniform grids. For clarity, the spikes at the reference node are masked and the plots are shifted with respect to the potential at $x = 0{\cdot}0$. Notice once again that the potential obtained by Method 1 is negative and of opposite sign to the exact solution, and the convergence rate appears to be quite slow. On the other hand, the solution obtained by Method 2 experiences an undershoot in the profile before the spike runs off, and the convergence rate seems to be faster. Finally, Method 3 produces an acceptable result, even when using a low resolution, and converges quickly to the exact solution as the mesh is refined.

Having selected Method 3 for conditioning the singular matrix, we now present the results from the singular and regularized formulations of the velocity and its gradients in the domain interior, and compare them with the exact solution. Figure 4(a) represents the parametric study of the singular and regularized formulations for $w$ along the ($0{\cdot}001 \leqslant x \leqslant 0{\cdot}999$, $0{\cdot}5$, $0{\cdot}9999$) station. Figure 4(b) represents the corresponding $u$ component. At all resolutions the agreement between the approximations and the exact solution is excellent. Interestingly, the singular and regularized formulations produce identical results for all grid resolutions, even at such a close proximity to the boundary. This is because the integrations are performed exactly and in closed form. However, as the field point moves closer to the boundary, the two profiles are expected to diverge from each other because of the difference in the singularity orders of the integrations—the more singular integrals will cease to exist farther away from the boundary. Figure 4(c) shows a comparison between the singular and regularized formulations for the variation of $w$ along ($0{\cdot}5$, $0{\cdot}5$, $0{\cdot}001 \leqslant z \leqslant 0{\cdot}999$) at low resolution. The profiles are identical and agree well with the exact solution.

Figures 5(a) and 5(b) show the parametric studies of the singular and regularized approximations for $\partial u/\partial z$ along ($0{\cdot}001 \leqslant x \leqslant \leqslant 0{\cdot}999$, $0{\cdot}5$, $0{\cdot}9999$), respectively. The singular and exact solutions compare well within $0{\cdot}35 \leqslant \leqslant x \leqslant \leqslant 0{\cdot}65$, but outside this region the approximations become quite oscillatory and quickly diverge within $0{\cdot}1$ of the boundary. On the other hand, the regularized solutions display very mild oscillations, are bounded near the boundary and improve with an increase

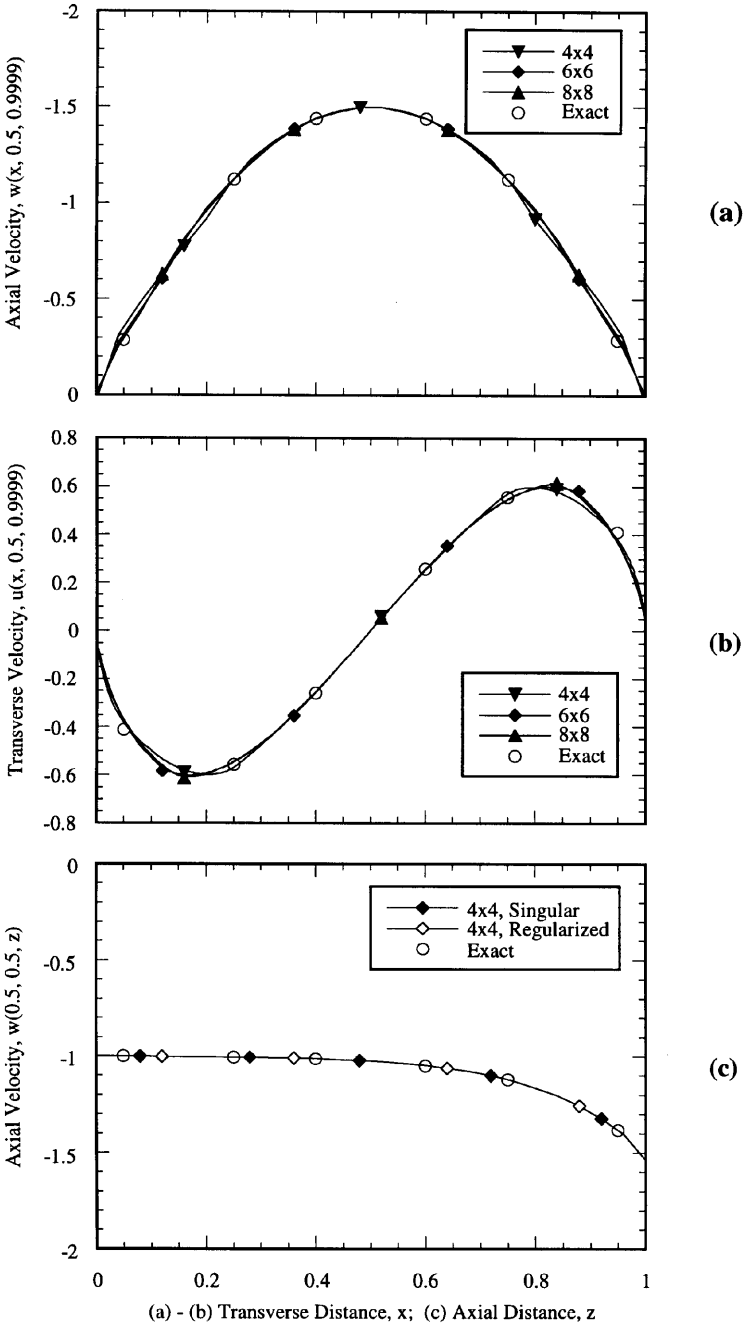


Figure 4. Parametric comparison between singular and regularized integral formulations for the velocity in the interior. The two formulations produce identical profiles. Method 3 was used in all cases to condition the matrix

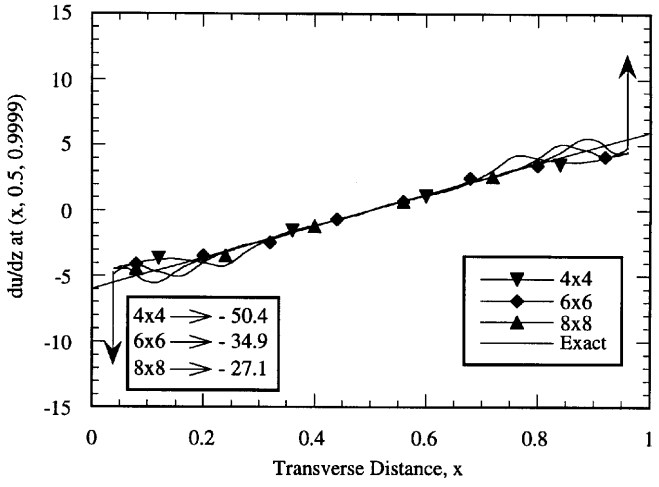


(a)

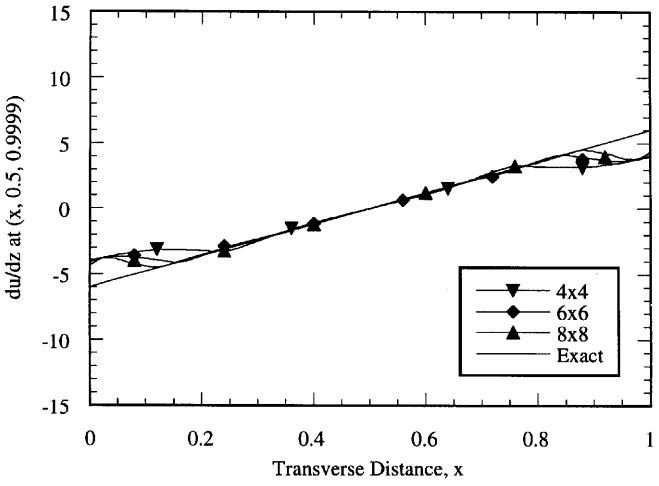


(b)

Figure 5. Parametric comparison between (a) singular and (b) regularized formulations for $\partial u/\partial z$ in cross-flow direction. Method 3 was used in all cases to condition the matrix

in the grid resolution. Considering that the exact solution is discontinuous at the boundary and that it takes over 800 terms in the series solution to obtain a non-oscillatory profile near the boundary, the regularized formulation is doing very well.

Figure 6 depicts the parametric study of the singular and regularized approximations of $\partial u/\partial x$ along $(0{\cdot}5,\ 0{\cdot}5,\ 0{\cdot}001 \leqslant \leqslant z \leqslant \leqslant 0{\cdot}999)$. The singular integrations diverge at both ends of the domain, but the approximations improve with an increase in the grid resolution. On the other hand, the regularized profiles and the exact solution are indistinguishable, even at the low resolution.

Having demonstrated the accuracy of the regularized formulation for the velocity gradients, we re-examine the three matrix conditioning methods to determine how deeply, if at all, the contamination from the spike penetrates into the domain. Figure 7(a) depicts the effect of the three matrix

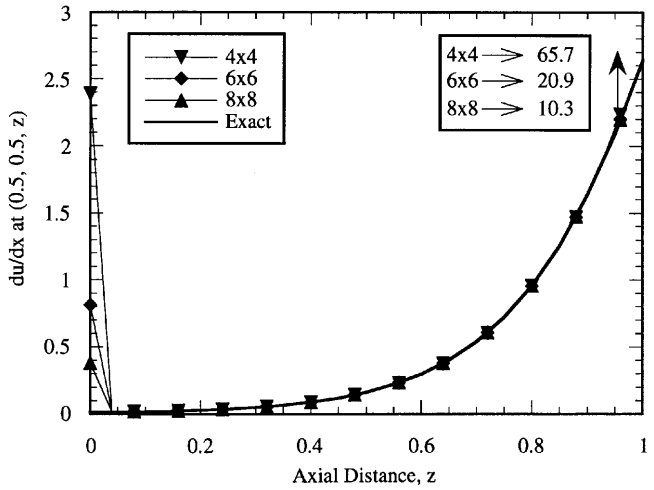


Figure 6. Parametric comparison between singular and regularized integral formulations for $\partial u/\partial x$ in the streamwise direction. Method 3 was used in all cases to condition the matrix. Profiles with symbols were obtained using the singular formulation. The regularized profiles are identical with the exact solution

conditioning methods on the regularized $w$ profile along (0·5, 0·5, $0{\cdot}001 \leqslant z \leqslant 0{\cdot}999$). Figures 7(b) and 7(c) represent similar studies for $\dfrac{\partial u}{\partial x}$ and $\dfrac{\partial v}{\partial y}$, respectively. Only the results from the case using $8 \times 8$ uniform grid distribution are presented here—the lower resolutions display the same trend. Notice that the spike seems to have only a local effect in Method 2; nevertheless, the flow variables—especially the velocity gradients—diverge in the vicinity of the reference point. The influence of the spike on the flow field is more pronounced in Method 1, where it causes a strong flow reversal towards the exit and contaminates the velocity gradients everywhere in the field. The clear conclusion from these parametric studies is that the use of the pseudo-Lagrange multiplier is necessary for obtaining an accurate description of the potential flow and that the standard elimination technique produces the poorest-quality results.

## CONCLUSIONS

The solution of the 3D internal Neumann problem and the evaluation of the potential velocity and its gradients at arbitrary locations inside the domain are essential ingredients of a grid-free random vortex methodology for the simulation of high-Reynolds-number incompressible flow in 3D geometries. The Neumann problem is used to impose the normal flux boundary condition, while the velocity gradients are used to evaluate the vorticity stretch in the field. We propose using the direct boundary element method for this purpose in order to preserve the grid-free nature of the solution and to eliminate the complexity associated with volumetric meshing.

It was shown in this paper that removing the matrix singularity, which arises from the discretization of the Neumann problem, by traditional methods leads to a localized spike for the potential at the eliminated node—in turn yielding unphysical flow results in the domain interior. A pseudo-Lagrange multiplier was subsequently added to the matrix to smooth out the discretization errors and was shown to produce accurate results.

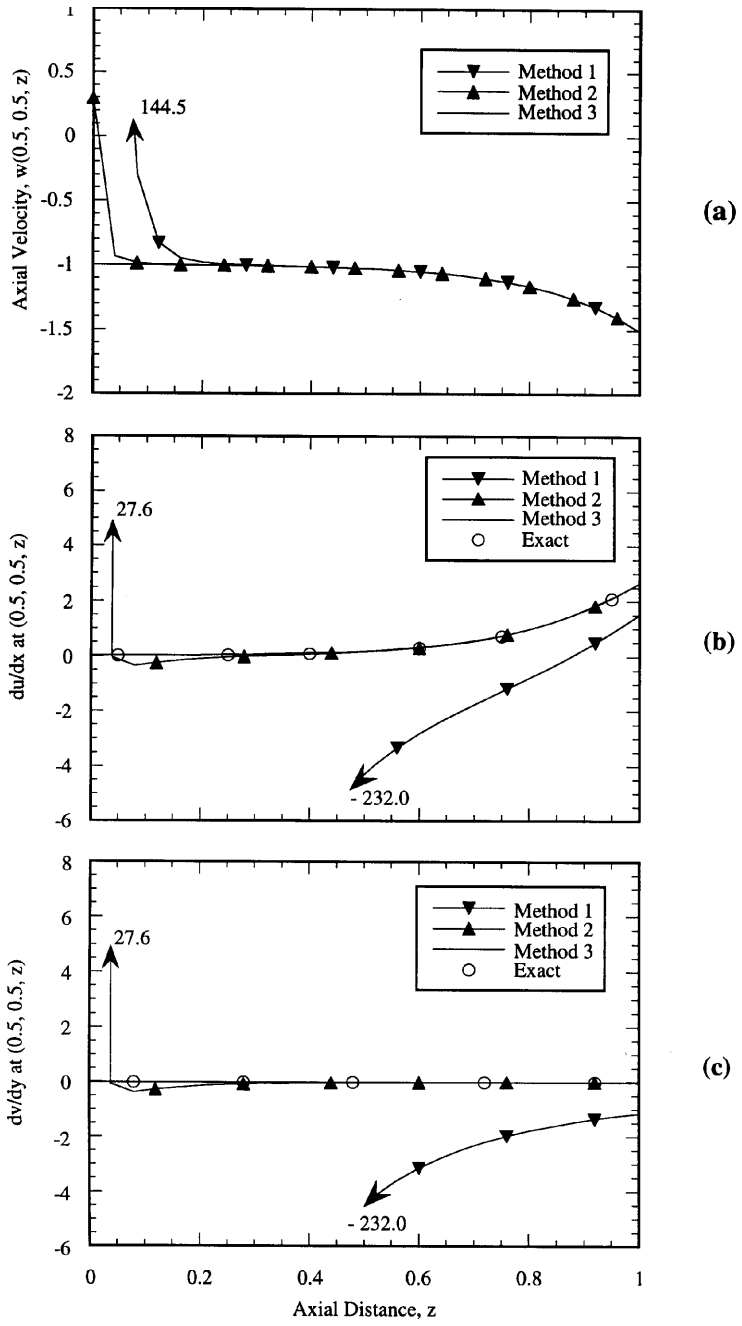


Figure 7. Parametric study of the flow field in the interior using three matrix conditioning methods. Regularized integral formulations were used in all cases

Additionally, it was shown that the classical derivation for the velocity gradients, which has fourth-order integrand singularity, yields highly inaccurate gradient values near the boundary. Inaccurate velocity gradients directly affect the stretch term in the random vortex computations and will lead to poor predictions of the flow field and possibly numerical instability. Thus a regularized integral formulation of the velocity gradients was developed which reduces the order of the singularity by two. The singular formulation of the velocity gradients was shown to diverge at approximately 0·1 normalized units away from the boundaries, whereas the regularized version remained bounded at as close as 0·001 normalized units.

The regularized integral formulation for the velocity gradients requires the potential distribution to be twice-differentiable. Thus, in this paper, piecewise quadratic interpolation functions were used to approximate the variations of the potential and normal flux over plane triangular elements. The singular integrations were performed in closed form and are listed in the Appendix.

Finally, two independent node numbering systems were applied to the boundary potential and its normal flux—a regular noding system to describe the single-valued potential and a multiple-node concept to specify the multi-valued normal fluxes at the boundary edges and corners. This scheme was shown to yield accurate boundary potential solutions and to reduce memory and CPU cost requirements significantly.

ACKNOWLEDGEMENTS

This project was funded by Ford Motor Company. All numerical tests were conducted on the Cray C90 at the Pittsburgh Supercomputing Center. The first author wishes to thank Dr. Daniel Medina for providing us with the computer code to evaluate the singular integrals across linear triangles.

## APPENDIX

Here we present the recursive formulae for the integral evaluations. The recursions stop where the integrals can conveniently be looked up from a table or be evaluated by a symbolic mathematics package.

### *Integrations of type* $\frac{1}{r}m$

The details of the integrations of type $\int_{\partial\Omega} \mathrm{d}S/r^m$ are given in Reference 8 for $m = 1$, 3 and 5. In this paper we present a pseudo-recursive approach to simplify the computations and extend it to cases $m = -1$ and 7, which are necessary for the quadratic integrations and the singular evaluation of the velocity gradients, respectively.

The basic idea proposed by Medina and Liggett[8] is to convert the area integral into a counter-clockwise line integral around the perimeter of the element using the divergence theorem. Since the integrals must be carried out along each element side, a local two-dimensional co-ordinate system $s$ is used for each side in the $\xi$–$\zeta$ plane; $s$ is parallel to the side and $t$ is normal to it, as depicted in Figure 8(a). The $I^1$ integral is

$$I^1 \equiv \int_{\partial\Omega} \frac{\mathrm{d}S}{r} \equiv -\sum_{i=1}^{3}\left( t_i \int_{s_{i,1}}^{s_{i,2}} \frac{r_i^2 \, \mathrm{d}r_i}{(r_i^2 - \eta^2)\sqrt{(r_i^2 - \eta^2 - t_i^2)}} \right) + \eta\theta,$$

where $i$ denotes the element side, and $s_{i,1}$ and $s_{i,2}$ represent the beginning and end points of each line segment, respectively. $\theta$ is a two-dimensional angle which accounts for the integral singularity when $\mathbf{x}$ falls into or on the triangle: $\theta = 2\pi$ if $\mathbf{x}$ falls inside the triangle; $\theta = \pi$ if $\mathbf{x}$ falls on the perimeter of the triangle—excluding the vertices; $\theta = 0$ if $\mathbf{x}$ is outside the triangle; and $\theta$ is equal to the angle of the vertex if $\mathbf{x}$ falls on the vertex. The individual integrals are obtainable from the tables. The other

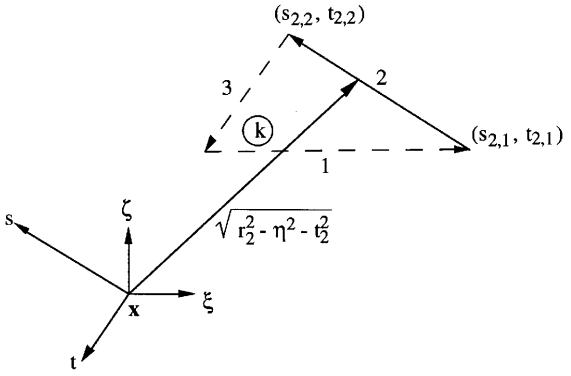


(a)

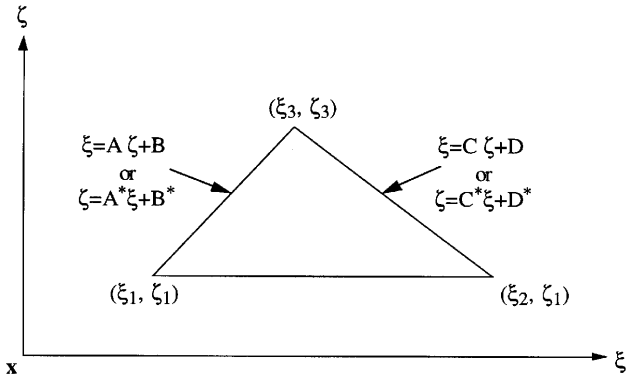


Figure 8. Schematic diagram of the local co-ordinate system used in the singular integrations

integrals are

$$I^{-1} \equiv \int_{\partial\Omega} r \, \mathrm{d}S \equiv \frac{\eta^2 I^1}{3} - \frac{1}{3}\sum_{i=1}^{3}\left( t_i \int_{s_{i,1}}^{s_{i,2}} \frac{r_i^2 \, \mathrm{d}r_i}{\sqrt{(r_i^2 - \eta^2 - t_i^2)}}\right),$$

$$I^3 \equiv \int_{\partial\Omega} \frac{\mathrm{d}S}{r^3} \equiv -\frac{I^1}{\eta^2} - \frac{1}{\eta^2}\sum_{i=1}^{3}\left( t_i \int_{s_{i,1}}^{s_{i,2}} \frac{\mathrm{d}r_i}{\sqrt{(r_i^2 - \eta^2 - t_i^2)}}\right),$$

$$I^5 \equiv \int_{\partial\Omega} \frac{\mathrm{d}S}{r^5} \equiv \frac{I^3}{3\eta^2} - \frac{1}{3\eta^2}\sum_{i=1}^{3}\left( t_i \int_{s_{i,1}}^{s_{i,2}} \frac{\mathrm{d}r_i}{r_i^2\sqrt{(r_i^2 - \eta^2 - t_i^2)}}\right),$$

$$I^7 \equiv \int_{\partial\Omega} \frac{\mathrm{d}S}{r^7} \equiv \frac{3I^5}{5\eta^2} - \frac{1}{5\eta^2}\sum_{i=1}^{3}\left( t_i \int_{s_{i,1}}^{s_{i,2}} \frac{\mathrm{d}r_i}{r_i^4\sqrt{(r_i^2 - \eta^2 - t_i^2)}}\right).$$

*Integrations of type* $\xi^i\zeta^j/r^m$

In this subsection we present the recursive formulae for all the other integrals. Figure 8(b) is the accompanying diagram defining the notations used in the integrals:

$$I^m_{\xi} \equiv \frac{1}{2-m}\int_{\zeta_1}^{\zeta_3}\frac{1}{r^{m-2}}\bigg|_{\xi=A\zeta+B}^{\xi=C\zeta+D} \mathrm{d}\zeta, \qquad I^m_{\zeta} \equiv \frac{1}{2-m}\left(\int_{\xi_1}^{\xi_3}\frac{1}{r^{m-2}}\bigg|_{\zeta=\zeta_1}^{\zeta=A^*\xi+B^*} \mathrm{d}\xi + \int_{\xi_3}^{\xi_2}\frac{1}{r^{m-2}}\bigg|_{\zeta=\zeta_1}^{\zeta=C^*\xi+D^*} \mathrm{d}\xi\right),$$

$$I^m_{\xi^2} \equiv \frac{1}{2-m}\int_{\zeta_1}^{\zeta_3}\frac{\xi}{r^{m-2}}\bigg|_{\xi=A\zeta+B}^{\xi=C\zeta+D} \mathrm{d}\zeta + \frac{1}{m-2}I^m_1, \qquad I^m_{\xi\zeta} \equiv \frac{1}{2-m}\int_{\zeta_1}^{\zeta_3}\frac{1}{r^{m-2}}\bigg|_{\xi=A\zeta+B}^{\xi=C\zeta+D} \zeta\,\mathrm{d}\zeta,$$

$$I^m_{\zeta^2} \equiv I^{m-2}_1 - \eta^2 I^m_1 - I^m_{\xi^2}, \qquad I^m_{\xi^3} \equiv I^{m-2}_{\xi} - \eta^2 I^m_{\xi} - I^m_{\xi\zeta^2},$$

$$I^m_{\xi^2\zeta} \equiv \frac{1}{2-m}\int_{\zeta_1}^{\zeta_3}\frac{\xi}{r^{m-2}}\bigg|_{\xi=A\zeta+B}^{\xi=C\zeta+D} \zeta\,\mathrm{d}\zeta + \frac{1}{m-2}I^{m-2}_{\zeta}, \qquad I^m_{\xi\zeta^2} \equiv \frac{1}{2-m}\int_{\zeta_1}^{\zeta_3}\frac{1}{r^{m-2}}\bigg|_{\xi=A\zeta+B}^{\xi=C\zeta+D} \zeta^2\,\mathrm{d}\zeta,$$

$$I^m_{\zeta^3} \equiv I^{m-2}_{\zeta} - \eta^2 I^m_{\zeta} - I^m_{\xi^2\zeta}, \qquad I^m_{\zeta^4} \equiv I^{m-2}_{\xi^2} - \eta^2 I^m_{\zeta^2} - I^m_{\xi^2\zeta^2},$$

$$I^m_{\xi^3\zeta} \equiv \frac{1}{2-m}\int_{\zeta_1}^{\zeta_3}\frac{\xi^2}{r^{m-2}}\bigg|_{\xi=A\zeta+B}^{\xi=C\zeta+D} \zeta\,\mathrm{d}\zeta + \frac{2}{m-2}I^{m-2}_{\xi\zeta}, \quad I^m_{\xi^2\zeta^2} \equiv \frac{1}{2-m}\int_{\zeta_1}^{\zeta_3}\frac{\xi}{r^{m-2}}\bigg|_{\xi=A\zeta+B}^{\xi=C\zeta+D} \zeta^2\,\mathrm{d}\zeta + \frac{1}{m-2}I^{m-2}_{\zeta^2},$$

$$I^m_{\xi\zeta^3} \equiv I^{m-2}_{\xi\zeta} - \eta^2 I^m_{\xi\zeta} - I^m_{\xi^3\zeta}, \qquad I^m_{\zeta^4} \equiv I^{m-2}_{\zeta^2} - \eta^2 I^m_{\zeta^2} - I^m_{\zeta^2\zeta^2}.$$

## REFERENCES


1. A. Gharakhani and A. F. Ghoniem, *J. Comput. Phys.*, submitted.
2. G. K. Batchelor, *An Introduction to Fluid Dynamics*, Cambridge University Press, London, 1967.
3. P. K. Banerjee and R. Butterfield, *Boundary Element Methods in Engineering Science*, McGraw Hill, New York, 1981.
4. J. Balas, J. Sladek and V. Sladek, *Stress Analysis by Boundary Element Methods*, Elsevier, Amsterdam, 1989.
5. V. Sladek and J. Sladek, *Int. j. numer. methods eng.*, **33**, 1181 (1992).
6. V. Sladek and J. Sladek, *Int. j. numer. methods eng.*, **33**, 1481 (1992).
7. V. Sladek, J. Sladek and M. Tanaka, *Int. j. numer. methods eng.*, **36**, 1609 (1993).
8. D. E. Medina and J. A. Liggett, *Int. j. numer. methods eng.*, **26**, 2319 (1988).
9. A. Gharakhani, *Sc.D. Thesis*, Department of Mechanical Engineering, MIT, Cambridge, MA, 1990.
10. D. W. Kelly, G. G. W. Mustoe and O. C. Zienkiewicz, in *Developments in Boundary Element Methods—1*, P. K. Banerjee and R. Butterfield (eds), Applied Science, London, 1979.